RSC Advances

ROYAL SOCIETY
OF **CHEMISTRY**

www.rsc.org/advances

Three Way Electron Transfer of C-N-S Tri Doped Two-Phase Junction of TiO₂ Nanoparticles for Efficient Visible Light Photocatalytic Dye Degradation

S. Amreetha[†], S. Dhanuskodi[†*], A. Nithya[‡] and K. Jothivenkatachalam[‡]

[†]Nonlinear Optical Materials Laboratory, School of Physics, Bharathidasan University, Tiruchirappalli 620 024, Tamil Nadu, India

[‡]Department of Chemistry, Anna University, BIT Campus, Tiruchirappalli 620 024, Tamil Nadu, India

Abstract

C-N-S tridoped TiO₂ nanoparticles were synthesized by sol-gel method using thiourea as a source compound of carbon (C), nitrogen (N) and sulphur (S). 15 Wt% of thiourea has been used for effective dopants with different annealing temperatures (300, 400, 500 and 600˚C). X-ray diffraction results show that tridoping with C-N-S could effectively restrain the phase transformation of anatase to rutile at higher annealing temperature (600˚C). The size-strain plot method indicates that the crystallite size decreases from 32 to 9 nm with the addition of dopants. Fourier transform infrared analysis shows that the peaks observed at 1384, 1128 and 1051 cm^{-1} is attributed to N-H bond, bidentate S-O coordination to Ti^{4+} and Ti- O- C bond. UV-Vis study reveals that C-N-S tridoped TiO₂ is redshifted compared to pure. From the Photoluminescence spectra the band edge emission is redshifted with the different excitation wavelengths (280- 320nm). Enhancement of Rhodamine B dye degradation is observed for C-N-S tridoped TiO₂ nanoparticles (99% at 180 minutes) compared with undoped TiO₂ under visible light irradiation.

Keywords: Non-metal dopants in TiO₂, Photocatalytic activity, Dye sensitization, Mixed phase of anatase-rutile, Rhodamine B

1.   Introduction

Environmental pollution is becoming an increasingly serious threat for the ecosystem. The rapid unregulated industrial growth has led to the environmental pollution. The untreated release of toxic agents and industrial waste into air and water ways have resulted in pollution related diseases, global warming and climate changes. Photocatalysis provides a clean and cost effective method for the oxidation of organic pollutants. It is facilitated by the highly

oxidizing free O^{2-} and OH^- radicals which are produced by photogenerated electrons and holes.

TiO$_2$ is one of the most promising photocatalysts which has attracted considerable attention in recent years due to its high oxidative power and chemical stability[1-4]. However the wide bandgap (3.2 eV) and relatively high recombination rate of photogenerated electron-hole pairs have limited its photocatalytic activity. Doping narrow downs the bandgap via an electronic coupling effect between the dopant and TiO$_2$ or introduce some impurity energy level just above the valence band or just below the conduction band of TiO$_2$. For these purposes, various kinds of dopants such as nonmetals (C, N, S, F, P), metals (Fe, Cu, Mn, Co), noble metals (Au, Ag, Pt) and rare earths (La, Er, Y, Cr, Eu) have been attempted[5-8]. However, several authors have reported that the metal doping in TiO$_2$ has considerable drawbacks. It shows thermal instability and the metal centre acts as an electron trap which encourages the recombination of photogenerated electron hole pairs.

Doping in TiO$_2$ with anionic nonmetals such as carbon (C), nitrogen (N), sulfur (S), boron (B) and fluorine (F) has received much attention compared to cationic doping due to the significant reduction of recombination centres and narrowing the bandgap in the visible region[9-14]. The impurity state near to the valence bandedge does not act as charge carrier. The acid surface of N-S co-doped TiO$_2$ is proven for the adsorption of reactant molecules and it also acts as an electron acceptor to enhance the separation of photogenerated electrons and holes.

2. Experimental Section

2. 1. Synthesis of C-N-S doped TiO$_2$ nanoparticles

Titanium tetra isopropoxide (20 ml), isopropanol (60 ml), double distilled water (40 ml) and thiourea (15 wt %) were added and stirred for 6 hours at 303 K. The homogeneous solution was dried at 80°C in an oven until a dry gel was obtained. The procedure was repeated to prepare the undoped TiO$_2$ nanoparticles without the addition of thiourea. The undoped (P) and doped (D) TiO$_2$ nanoparticles were annealed at 300 (P1 & D1), 400 (P2 & D2), 500 (P3 & D3) and 600°C (P4 & D4).

2. 2. Characterization and Measurements

The crystalline structure was identified with a PAN analytical X'Pert PRO diffractometer with CuKα (λ = 1.5406Å) (X-ray diffraction (XRD) pattern). Fourier transform infrared (FTIR) spectra were recorded by KBr pellet method in a JASCO 460 PLUS spectrometer.

The presence of oxidation states is analysed by X-ray photoelectron spectroscopy (Shimadzu AXIS ULTRA-XPS). Morphology was observed by using a Field emission scanning electron microscope (FESEM) (QUANTA FEC 250). The diffuse reflectance spectra (DRS) were recorded with a Shimadzu UV - 2450 solid state with an integrated sphere assembly. The photoluminescence (PL) spectra were analyzed with a HORIBA Flouromax – 4 for the excitation wavelengths 280-320 nm. Photocatalytic experiments were carried out in a photocatalytic reactor. A 300 W tungsten halogen lamp (8500 lumen) was used as a visible light source (400-750 nm). 15 mg of photocatalyst was optimized and suspended in 50 ml of Rhodamine B (Rh B) solution (5 mg/L) under magnetic stirring. The mixture was kept in dark for 30 minutes to establish an adsorption – desorption equilibrium before the visible light irradiation. To demonstrate the reaching of equilibrium condition the mixture was (D4 catalyst) again kept in the dark upto 75 mints as shown in fig S1(Supporting information)**.** A small variation in the absorption for 30 and 75 mints indicates the enough time to reach adsorption/desorption equilibrium. The schematic diagram of photoreactor is shown in fig **S2** (Supporting information)**.** Air was bubbled through the reaction solution for a constant supply of oxygen to enhance the production of radicals[15-17].

3. Results and Discussion
3.1.   XRD - Phase transition

Figure 1 shows the XRD pattern of undoped and C-N-S doped TiO_2 nanoparticles annealed at 300, 400, 500 and 600 ºC. The diffraction peaks become narrow with the improved degree of crystallinity at higher annealing temperatures. The phase content of TiO_2 is calculated using the formula:

$$X_A = \frac{1}{1 + \dfrac{I_R}{0.8 \times I_A}} \qquad (1)$$

 From the table 1, the 100% anatase phase is observed for the doped and undoped samples annealed upto 500ºC. The formation of rutile phase occurs at 600ºC. P4 and D4 show 86 and 12% of rutile phase respectively. Compared to the undoped samples, doped samples show broad diffraction peaks. These broad diffraction peaks arise due to the presence of high fraction of atoms/defects on the grain boundary[18]. The grain boundary containing defects causes lattice strain and inhibits the grain growth. The lattice strain (δ), stress (ε) and the

energy density (u) values are calculated by Size- Strain Plot (SSP) method[19] S3 (Supporting Information). The average crystalline size (D) was estimated using the Scherrer equation:

$$D = \frac{K\lambda}{\beta \cos\theta} \qquad (2)$$

Here, K is a constant that depends on the shape of the particles; for spherical particles it is 3/4, λ – wavelength of X-ray, β- full width half maximum and θ – glancing angle. The strain and the stress values are calculated by the equation,

$$(d_{hkl} \beta_{hkl} \cos\theta)^2 = K/D (d^2_{hkl} \beta_{hkl} \cos\theta) + (\epsilon/2)^2 \qquad (3)$$

$d^2_{hkl} \beta_{hkl} \cos\theta$ is plotted against $(d_{hkl} \beta_{hkl} \cos\theta)^2$ and after linear fitting the slope gives the D value and the root of the intercept gives the strain (δ) value as shown in table 1. Stress (ϵ) and energy density (u) values are calculated from the strain. A decrease in defects at grain boundary and increase of crystallite size reduces the stress (ϵ), strain (δ) and energy density values (u) in TiO_2 lattice on heat treatment. The strain (δ) is high for the doped samples compared to the undoped. This is due to more number of oxygen vacancies created during the C-N-S dopants in TiO_2 lattice. The ionic radius of S^{2-}, S^{6+}, N^{3-}, Ti^{4+} and O^{2-} is 1.84, 0.30, 1.712, 0.68 and 1.3Å respectively. As mentioned above, the anionic sulfur doping is difficult to achieve whereas the substitution of Ti^{4+} by S^{6+} is chemically more favourable than the replacement of O^{2-} by S^{2-}. The charge compensation of Ti^{4+} by S^{6+} creates oxygen vacancy in TiO_2 lattice. In N-doped TiO_2, nitrogen atoms replace oxygen atoms due to the similar atomic radii and some occupies the interstitial position. The lattice expands along the c – axis and the increase of d-spacing indicate the incorporation of sulfur and nitrogen atoms in TiO_2 lattice as shown in figure S4 (Supporting Information). Whereas carbon atoms are most likely exist on the surface of TiO_2 lattice and form a layer composed of complex carbonate species resulting in the suppression of TiO_2 crystal growth[20].

3. 2. FTIR

FTIR spectra of the undoped and tridoped TiO_2 nanoparticles annealed at different temperatures are shown in figure 2. The absorption at 3429 and 1641 cm^{-1} are assigned to the stretching and bending vibration mode of the hydroxyl group. The intensity of these absorption bands reduces for further increase in the annealing temperatures. Ti-O stretching vibration peak is observed at 600 cm^{-1}. Symmetric carboxalate stretching frequency is observed at 1384 cm^{-1}. The surface adsorbed SO_4^{2-} species has a peak at 1128 cm^{-1} which is

assigned to the asymmetric stretching frequency of S=O bond. The peak at 1041 cm^{-1} is due to the nitrate or hyponitrate group[21]. The absence of peak at 3189 and 1400 cm^{-1} (NH^{4+}) reveals that nitrogen is present only in the form of nitrate or hyponitrate species.

3. 3. XPS Analysis

The XPS analysis was performed for D3 and D4 samples to confirm the presence of carbon, nitrogen and sulfur and its effect in TiO$_2$ lattice with respect to annealing temperature. In fig S5 (supporting information) the XPS spectrum of Ti 2p core level for D3 exhibits Ti 2p$_{3/2}$ peak at 459.2 eV and an O 1s peak at 530.4 eV. After annealing at 600˚C, Ti 2p$_{3/2}$ and O 1s peaks have been shifted to 458.8 and 530.0 eV respectively. Atomic percentage of nitrogen and sulfur doping increased with annealing temperature due to the more effective decomposition of thiourea[22] (Supporting Information- table 2). It has been reported that an increase in the covalent nature of the bond between Ti and N induces the formation of oxygen vacancies resulting in the shift of binding energies of Ti and O to the lower side[23-24].

N 1s peak at 399. 8 eV is ascribed to Ti-O-N or Ti-N-O oxynitride as sown in fig S6 (Supporting information). But it has been assigned to N-H or adsorbed NH$_3$ since its binding energy is close to the value of 398.7 – 399.7 eV cited from NH$_3$. In the present case, from the FTIR spectra no band characteristics of N-H or NH$_3$ have been found confirming the formation of Ti-O-N. Nitrogen can be located as interstitially or substitutionally into TiO$_2$ lattice. It has been reported that N 1s peak at 400 eV is typically assigned to the interstitial nitrogen dopant. The occupation of the N atoms in the TiO$_2$ lattice depends on the synthetic route. In general interstitial nitrogen doping is preferred under oxygen rich condition; whereas oxygen depleted conditions (at high reducing condition) substitutional N doping is favoured[25-26]. The present report reveals that N doped as in interstitial position in TiO$_2$ lattices.

Strong peak at 169 and 168.6 eV (D4) are assigned to S^{6+} (SO^{2-} states)[27-28]. These SO$_4^{2-}$ ions form S=O and O-S-O bonds on TiO$_2$ surface creating unbalanced charge on Ti vacancies/defects in the TiO$_2$ network. Meanwhile there is no peaks were found around 160-163 eV which indicates the absence of substitution of sulfur atoms by oxygen atoms as Ti-S bond. A broad energy range of C 1s spectrum observed from 282 to 291 eV which is well fitted to three peaks. The first peak at 285 eV (D3) is ascribed to the adventitious carbon spices from the XPS measurement itself. The second and third peaks at 286.5 and 289.3 eV are attributed to C-O and C=O bonds respectively[29]. A peak at 281 eV is not observed in this

study resulting from the formation of Ti-C bond. So the replacement of C atoms by the O atoms does not occur. The presence of C-O bonds (288.4 eV) indicates C atoms substitute some of the Ti atoms and forms Ti-O-C structure.

In most of the nonmetal doped TiO_2 nanomaterials the occupancy of nonmetal atoms probably in Ti site and located in the interstitial positions of TiO_2 lattices. When the nonmetal ions replace the Ti ions, a charge imbalance is created in the lattice. The extra charge is neutralized by the surface adsorbed hydroxyl molecules which will more beneficial for the photocatalytic activity[30].

3. 4. FESEM

The surface morphology of P4 and D4 were analyzed by FESEM as shown in figure S7 (Supporting Information). It illustrates that the particles are in irregular spherical shape and most of them got agglomeration on the surface which is due to the high annealing temperature. D4 shows very small size distribution of particles compared to P4 due to the doping effect as evidence from the XRD peak broadening analysis.

3. 5. UV-Vis Diffuse reflectance

 Fig 3 (a and b) shows the UV-Vis absorbance spectra of undoped and C-N-S doped TiO_2 nanoparticles annealed at different temperatures. Bulk TiO_2 anatase and rutile phases have the bandgap of 3.2 and 3.0 eV respectively. The existence of dominant anatase phase in undoped and C-N-S doped TiO_2 nanoparticles shows the maximum absorption edge in the range of 330 nm except P4. Whereas the absorption edge of P4 is substantially shifted to 367 nm owing to the abundant percentage of rutile phase (86%) and it has the lower bandgap (3.0 eV) than the anatase (3.2 eV).The bandgap energies for the catalysts are determined by Kubelka – Munk function[31-32] as shown in fig S8 (Supporting information) and the calculated values are tabulated in table 2.   A noticeable red shift of bandgap is observed for the C-N-S doped TiO_2 compared with undoped nanoparticles. This red shift originates from the oxygen vacancies created during the doping process and also the mixing of N 2p + S 2p states[33] induce the local states near to the valence band edge and thus the oxygen vacancies create local state below the conduction band edge. Then the excitation from the local states to the conduction band enhances the absorption to the higher wavelength side. In addition, the bandgap is blue shifted for D4 when the annealing temperature is increased. This is attributed

to the enhancement of crystallinity and the consequent decrease of oxygen vacancies at the higher annealing temperature.

3. 6. Photoluminescence

PL spectra have been widely used to disclose the efficiency of charge carrier trapping, migration and transfer of an electron hole pairs in materials. The PL spectra of undoped and C-N-S doped TiO_2 nanoparticles annealed with different temperatures taken under different excitation wavelengths 280, 290, 300, 310 and 320 nm. The PL peak positions of all samples are the same under the same excitation wavelengths as shown in fig 4 (a and b). Emissions on semiconducting materials arise from radiative recombination of photogenerated electrons and holes and then the surface defects related photoluminescence[34]. When the semiconductor is excited by the photons with the energy equal/greater than the bandgap of the material, the photogenerated electrons can transfer from the conduction band (CB) to the valence band (VB) with the release of radiative energy. This process is called as direct band to band transition or near band edge emission (NBE). In this study the NBE observed at 384 and 403 nm for anatase and rutile TiO_2 respectively. The phenomenon of NBE is different for anatase and rutile phases. It has been reported that the single crystalline rutile TiO_2 emits free excitons whereas self trapped excitons (STE)[35-37] in anatase since the coordination number of rutile is the largest (two edges and eight corners) compared to anatase (eight corners only). On the other hand, the excited electrons first transfer from the conduction band to different sub-bands such as surface oxygen vacancies or defects via non radiative transition and later transfer from sub-bands to the valence band via radiative transition with the release of energy. This process is related to the shallow traps and the corresponding emission observed in the visible region since the oxygen vacancy or defect states are located first below the lower end of the conduction band at 0-1eV. The peak centred at 468 nm observed for both anatase and rutile TiO_2, which are relate with the shallow traps on surface oxygen vacancies. It should be noted that the PL intensity increases with the annealing temperature. However, the crystallinity of TiO_2 nanoparticles increases with annealing temperature and it cause the reduction in the density of the defect states. As a result, the trapping of an electron in the defect states decreased in which the non-radiative transition of photoexcited charge carriers were diminished, thus the enhancement of luminescence observed.

Moreover from fig 5 (a and b) the PL spectra of all the samples are redshifted with increasing excitation wavelength[38] from 280 – 320 nm. Rutile phase (P4) shows a small variation with

the excitation wavelength (5 nm) but for the anatase phase it shows 16 nm. In this case the shift of the PL band cannot be due to the existence of energetically different kinds of molecules and its excited state relaxation process. PL emission and excitation spectra have a dependence on the particle size. In this way, the crystallite size of rutile particles at the higher annealing temperature will be even whereas for the anatase phases the crystallite sizes are very tiny and it cannot be even at the surfaces due to the quantum size effect.Meanwhile, when irradiated by a shorter wavelength light electrons in anatase phase TiO_2 nanoparticles especially in some smaller particles will be excited to the CB. Since the defects level keep the same and the radiative transition will occur i.e. the relaxation of electrons from CB to the defect level will emit photons with a larger energy (shorter wavelength). When increasing the excitation wavelength, electrons only in larger particles are excited and it emits light with longer wavelength that is emission red shifts with increasing excitation wavelength. At the same time, when the excitation wavelength exceeds 330 nm, the number of sensitive particles decreases quickly, as a result the emission intensity drops and the red shift get saturated.

3. 7. Photocatalytic Study

The visible light photocatalytic activity of undoped and C-N-S doped TiO_2 nanoparticles annealed at different temperatures was examined by the degradation of Rh B. Temporal changes in the concentration of RhB were monitored by examining the absorption in the UV-Vis spectra at 553 nm as shown in fig (6). The percentage of dye degradation efficiency of all the samples are shown in fig (7).The photodegradation efficiency of Rh B was calculated by the reaction rate constant k, i.e. ln (C/C_o) = kt, with C_o and C being the initial and final reaction concentrations of Rh B respectively[39] (fig 8). C-N-S doped TiO_2 has the highest apparent reaction rate constant which is 2.3 times that of undoped one. It is due to the doping effect and also it helps to maintain 86% of anatase and 14% of rutile phases in TiO_2 lattice. The mechanism of the TiO_2 – mediated photodegradation of Rh B described by two competitive pathways: an dealkylamine (de-ethylation of Rh B, the DE path) and the cleavage of the whole conjugated chromophore structure (the CC path). In general, cleavage of the Rh B ring structure caused by the weakening of the absorption band, and the gradual hypochromic shift[40] (blue shift) of the absorption maximum (553 nm) is related to the N-de-ethylation of Rh B molecules. To differentiate between DE and CC path, temporal UV- Vis absorption spectra of Rh B were recorded for P4 and D4. To identify the degradation pathway, the graph is plotted for the change of hypsochromic shift ($\Delta\lambda$) versus the change of the normalized maximum absorption ΔAn (= Abs max/ A0 max) of P4 and D4 (fig 9). Rh B

dye degraded by 2-step process[41] as indicated in the fig (10). In stage I, a small variation of $\Delta\lambda$ reveals that the CC path in the early stage of photodegradation; then the exponential rise in the stage II suggests that predominating the DE path. From the (fig 10) the wavelength shift is observed which is evident that the de-ethylation of Rh B because of attack by one of the active oxygen species on the N-ethyl group. But the variation of wavelength shift is less for P4 compared to D4. Rh B is de-ethylated in a stepwise manner i.e. ethyl group is removed one by one as confirmed by the gradual wavelength shift towards the blue region. De-ethylation of the fully N, N, N^1, N^1-tetraethylated Rhodamine B has the wavelength at 553 nm; and it shifts to lower wavelength 536 nm for N, N, N^1-tri-ethylated; N, N^1-di-ethylated Rh B is 527 nm; N-ethylated Rh B is at 510 nm. In general fully ethylated Rh B has the peak shifts from 553 to 498 nm. In this study largest wavelength shift is observed from 553 to 510 nm which means that the major contribution of Rh B degradation is DE path[42].

Catalyst Variation

Figure S9 (Supporting Information) shows the kinetics graph of different catalyst amounts of D4. It is evident that initially photodegradation rate increases with an increase in the amount of photocatalyst and then decreases with increase in catalyst concentration. The addition of higher quantities of catalyst does not give further enhancing effect on the degradation efficiency while the adsorption of dye molecules saturated on the surface of the photocatalyst; and the excess of catalyst particles may increase opacity of the suspension which may retard the degradation rate, and then it enhances the particle- particle interaction caused the collision with ground state catalyst and hence decrease in dye concentration[43]. Photocatalytic activity is done for bare Rh B as shown in figure S10 (Supporting Information). There is no much variation in absorption spectra after 180 mints irradiation which confirms that the observed degradation is mostly due to photocatalyst.

Mechanism Discussion

Pathway I

 A probable mechanism about the photodegradation of Rh B is illustrated in fig (11). The mechanism of photoassisted degradation of organic dyes in aqueous TiO_2 dispersion under visible light irradiation is different from the UV light illumination. In the visible light irradiation, the dye get excited from the ground state to the triplet excited state (dye*). The dye sensitization process is usually referred to as indirect mechanism. It is generally prevalent and much faster reaction over direct mechanism (UV-light illumination). The dye

sensitization involves multiexponential excitation kinetics i.e. from the singlet excited state of the dye to the TiO_2 conduction band (CB) (femtoseconds) and the excitation from triplet excited states of the dye to the TiO_2 CB (picoseconds). In this process, dye get excited rather than TiO_2 CB to appropriate singlet and triplet states, and thus dyes are subsequently converted to cationic dye radicals[44-47]. Then the electrons are injected to the TiO_2 CB. The proposed equation is as follows,

$$dye + h\nu \rightarrow dye^*$$
$$dye^* + TiO_2 \rightarrow dye^{+\bullet} + TiO_2(e^-)$$

$$O_2 + e^-(CB) \rightarrow O_2^-(ads)$$
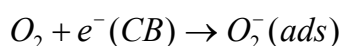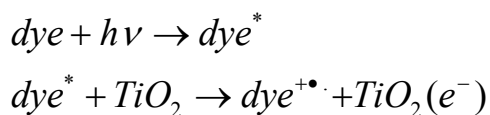
Electrons in the conduction band of TiO_2 (e⁻ CB) reacts with the surface adsorbed oxygen to produce anionic superoxide radical (O_2^-). This superoxide (O_2^-) forming hydroperoxyl radical ($^\bullet OOH$) by protonated H^+ ion and then subsequently produced H_2O_2 which further dissociates into highly reactive hydroxyl radical ($^\bullet OH$). Subsequently, the dye reacts with highly potential radical ($^\bullet OH$) which results in complete mineralization of dye with the formation of water followed by intermediates[48].

$$O^{2-}(ads) + H^+ \Leftrightarrow {}^\bullet HOO(ads)$$
$$2{}^\bullet HOO \rightarrow H_2O_2 + O_2$$
$$O^{2-} + e^- + 2H^+ \rightarrow H_2O_2$$
$$H_2O_2 + e^- \rightarrow {}^\bullet OH + OH^-$$
$$dye^{+\bullet} + O_2(O_2^- or {}^\bullet OH) \rightarrow dyeproducts$$
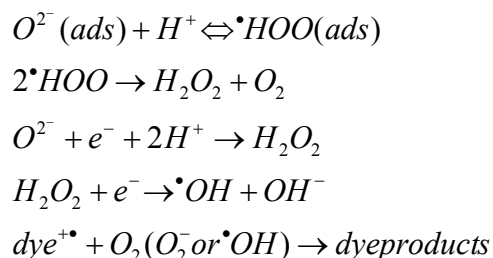
Pathway II

In the meantime, mixed state of N 2p+ S 2p modifies the electronic band structure of TiO_2. The O 2p orbital of TiO_2 mixes with N 2p and S 2p orbitals, resulting in bandgap narrowing[49-51]. The electrons are excited directly from this intermediate sates to CB of TiO_2 under visible light irradiation, generating O_2^- radicals similar to pathway I. However, in the mixed phase of anatase- rutile (D4), one of the crystal phases sensitizes the transfer of a photoinduced electron to other phase depending on the relative positions of the bandedge[52-56]. This solid-solid interface facilitates charge separation to suppress the electron-hole pair recombination. Two different mechanisms on the interfacial charge transfer pathways[57] of

anatase and rutile have been proposed by Roger et al.[58] and Deanna et al.[59] According to Roger et al., the rutile phase serves as a passive sink, hindering the recombination in the anatase phase. In this mode the electron transfer from CB of anatase to CB of rutile as rutile CB lies 0.2 eV below the CB edge of anatase titania. However, Deanna et al., explained the electron transfer from the rutile CB edge to electron trapping sites of anatase and subsequent transfer to lattice trapping sites favours effective charge separation. Since this process is energetically more favour due to the lattice trapping site of anatase is 0.8 eV lower in energy than the anatase CB which is even lower than the CB of rutile. When the CB of an anatase particle obtains an electron from rutile or VB itself, its Fermi level will shift towards more negative potential value, forming a Fermi level gradient. It also noted that the surface of anatase has a higher adsorption affinity to O_2 and more efficient for O_2 reduction than that of rutile. This superoxide anion helps to prevent the electron - hole pair recombination process in which maintaining electron neutrality within the TiO_2 molecule.

Meanwhile, the holes migration from VB of anatase to rutile where it lies 0.39 eV lowers than rutile. Then the photogenerated holes at the valence band of TiO_2 react with water to produce $^\bullet OH$ radical. This $^\bullet OH$ radical formed on the surface of the TiO_2 are extremely powerful oxidizing agent. It attacks adsorbed organic molecules or which are close to the catalyst surface causing them to mineralization[60-61].

$$h^+(VB) + H_2O(ads) \rightarrow {}^\bullet OH(ads) + H^+$$

$$\text{Or} \quad h^+(VB) + OH^- \rightarrow {}^\bullet OH$$
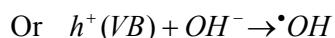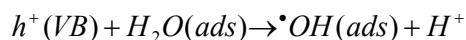
Pathway III

Under the visible light irradiation carbon on the TiO_2 surface acts as a photosensitizer. The excited photosensitized carbon injects an electron into the CB of TiO_2, producing O_2^- which is capable of degrading organic dyes similar to pathway I[62].

4. Conclusion

Highest photocatalytic activity for the degradation of Rhodamine B under the visible light irradiation was observed for the C-N-S doped TiO_2 nanoparticles annealed at 600°C. The existence of oxygen vacancies, formation of space charge – region at the anatase - rutile mixed phase, carbonaceous species at the surface of the TiO_2 and acidic surface of SO_4^- ions

are the main reasons for the enhanced photocatalytic activity of C-N-S doped TiO_2 nanocatalysts.

Author Information

Corresponding Author

Email: dhanus2k3@yahoo.com

Acknowledgement

Supporting Information. Adsorption – Desorption equilibrium determination, photocatalytic reactor, SSP – plot of undoped and C-N-S doped TiO_2 nanoparticles, d-spacing variation of undoped and C-N-S doped TiO_2 nanoparticles, XPS spectra of D3 and D4, FESEM images, Kubelka – Munk function, kinetics of catalyst optimization, Absorbance spectra of Rh B without catalyst, lattice parameters and the grain size of the synthesized TiO_2 nanoparticles and atomic percentage of C-N-S doped TiO_2 nanoparticles.

REFERENCES

1. S. Jenny, M. Masaya, T. Masato, Z. Yu. H. Jinlong, A. Masakazu and W. B. Detlef, *Chem. Rev,* **2014**, *114*, 9919-9986.

2. D. Rimeh, D. Patrick and R. Didier, *Ind. Eng. Chem. Res,* **2013**, *52*, 3581-3599.

3. L. Gomathi Devi and R. Kavitha, RSC *Adv,* **2014**, *4*, 28265 – 28299.

4. J. Zhang, Y. Wu, M. Xing, S. A. K. Leghari, and S. Sajjad, *Energy. Environ. Sci,* 2010, *3*, 715 – 726.

5. A. Ryoji, M. Takeshi, I. Hiroshi, and O. Takeshi, *Chem. Rev,* **2014**, *114*, 9824-9852.

6. X. Mingyang, W. Yongmei, Z. Jinlong, and C. Feng, *Nanoscale*, **2010**, *2*, 1233-1239.

7. J. Choi, H. Park and M. R. Hoffmann, *J. Phys. Chem. C,* **2010**, *114*, 783- 792.

8. W. Qingping, Z. Qiang and K. Roel van de, *J. Phys. Chem. C,* **2012**, *116*, 7219-7226.

9. V. Vaiano, O. Sacco, D. Sannino, P. Ciambelli, S. Longo, V. Vendittob and G. Guerrab**,** *J. Chem. Technol. Biotechnol*, **2014**, 89, 1175–1181.

10. G. Shang, H. Fu, S. Yang, and T. Xu, *Int. J. Photoenergy,* **2012,** 759306, 1-9.

11. K. Li, H. Wang, C. Pan, J. Wei, R. Xiong, and J. Shi, *Int. J. Photoenergy*, **2012,** 398508, 1-8.

12. O. Sacco, V. Vaiano, C. Han, D. Sannino, and D. D. Dionysiou, *Appl. Catal B, Environ*, **2015,**164, 462-474.

13. J. C. Yu, J. Yu, and J. Zhao, *Appl. Catal*, **2002**, 36, 31-43.

14. V. Vaiano, O. Sacco, M. Stoller, A. Chianese, P. Ciambelli and D. Sannino, *Int. J. Chem. Reac. Eng,* **2014**, 12, 1-13.

15. K. Jothivenkatachalam, S. Prabhu, A. Nithya and K. Jeganathan, *RSC. Adv,* **2014**, 4, 21221 – 21229.

16. A. Nithya, H. L. JeevaKumari, K. Rokesh , K. Ruckmani, K. Jeganathan and K Jothivenkatachalam, *J. Photochem. Photobio. B. Bio,* **2015**, 153, 412–422.

17. K. Jothivenkatachalam, S. Prabu, A. Nithya, S. Chandra Mohan and K. Jeganathan *Desalin. Water. Treat,* **2012**, 1- 12.

18. D. Chen, Z. Jiang, J. Geng, Q. Wang, and D. Yang, *Ind. Eng. Chem. Res,* **2007**, *46*, 2741 – 2746.

19. S. Amreetha and S. Dhanuskodi, *Spectrochimi. Acta Part A,* **2014**, 127, 543–549.

20. B. Choudhury and A. Choudhury, *International. Nano. Lett,* **2013**, *3*:55, 1-9.

21. Y. Guidong, J. Zheng, S. Huahong, X. Tiancin, and Y. Zifeng, *J. Mater. Che,* **2010**, *20*, 5302-5309.

22. P. Pradeepan, E. M. Declan, J. H. Steven and C. P. Suresh, *J. Phys. Chem. C,* **2009**, 113, 3246- 3253.

23. X. Ming-Yang, L. Wei-Kun, Wu. Yong – Mei, Z. Jin-Long and G. Xue-Qing *J. Phys. Chem. C,* **2011**, *115*, 7858-7865.

24. G. Ligang, D. Xiuquan, J. Haihui, M. Qinghu, Z. Guowei, T.Yan and L. Hong, *Cryst Eng Comm,* **2012**, *14*, 7662-7671.

25. W. Jin, N. T. De, P. L. James, H. Zhanglin, M. Ayyakannu, Z. Mingjia, Li. Ming, and Wu. Nianqiang, *J. Am. Chem. Soc,* **2009**, *131*, 12290-12297.

26. Y. Cong, J. Zhang and F. Cen, *J. Phys. Chem. C,* **2007**, *111*, 10618 – 10623.

27. Y. Wang, Y. Wang, Y. Meng, H. Ding, Y. Shan, Z. Xian and T. Xiaozhen, *J. Phys. Chem. C,* **2008**, *112*, 6620- 6626.

28. X. Quanjun, Y. Jiaguo and J. Mietek, *Phys. Chem. Chem. Phys,* **2011**, *13*, 4853–4861.

29. W. Xiaoyong, Y. Shu, D. Qiang, G. Chongshen, K. Takeshi and M. Jun-ichi, *J. Phys. Chem C,* **2013**, *117*, 8345 – 8352.

30. C. Yu. Jimmy, Ho. Wingkei, Yu. Jiaguo, Yip. Hoyin, K. W. Po, and Z. Jincai, *Environ. Sci. Techno,* **2009**, *39*, 1175-1179.

31. N. Ghobadi, *Int. Nano. Lett,* **2013**, 3:2, 1-4.

32. C. Yu and J. C. Yu, *Catal. Lett,* **2009**, 129, 462 – 470.

33. M. Yang, C. Hume, S. Lee, Y. H. Son and J. K. Lee, *J. Phys. Chem. C,* **2010**, *114*, 15292 – 15297.

34. B. Choudhury and A. Choudhury, *J. Lumin,* **2012**, *132*, 178–184.

35. I. Sildos, A. Suisalu, A. Aarik, T. Sekiya and S. Kurita, *J. Lumin,* **2000**, *87-89*, 290-292.

36. Z. Zhen, T. John, and J. Yates, *J. Phys. Chem. C,* **2010**, *114*, 3098-3101.

37. M. W. Jyh, C. S. Han and T. W. Wen, *J. Nano. Techno,* **2006**, *17*, 105-109.

38. I. Litty, K. Bindu, A. Deepthy and V. P. N. Nampoori, *J. Phys. D: Appl. Phys,* **2007**, *40*, 5670-5674.

39. S.T. Sapanbir, W. Guosheng, T. Min, and C. Aicheng, *J. Nanotechno,* **2012**, *23*, 475706-475714.

40. P. Periyat, S. C. Pillai, D. E. Mccormack, J. Colreavy and S. J. Hinder, J. *Phys. Chem,* **2008**, *112*, 7644-7652.

41. C. H. Cheng, C. H. Tzu and Y.L. Shan, *J. Appl. Sur. Sci,* **2013**, *280*, 171-178.

42. W. Taixing, L. Guangming and Z. Jincai, J. *Phys. Chem. B,* **1998**, *102*, 5845-5851.

43. A. Anila, M. Imran, R. M. Riffat, I. Hicham and A. N. Muhamaad, *RSC Adv*, **2014**, *4*, 37003-37026.

44. Z. He, W. Que, J. Chen, X. Yin, and Y. R. He, *J. ACS. Appl. Mater. Interfaces,* **2012**, *4*, 6816-6826.

45. A. T. Kuvarega, R. W. M. Krause and B. B. Mamba, *J. Phys. Chem. C,* **2011**, *115*, 2210 – 2220.

46. C. Chen, X. Li, W. Ma and J. Zhao, *J. Phys. chem. B,* **2002**, *106*, 318-324.

47. L. Haibei, W. Youngmei and Z. Jinlong, *J. ACS Appl. Mater. Interfaces,* **2011**, *3*, 1757-1764.

48. K. Avesh and T. Mohanty, *J. Phys. Chem. C,* **2014**, *118*, 7130−7138.

49. N. Serpone, *J. Phys. Chem,* **2006**, 110, 24287- 24293.

50. M. Sathish, B. Viswanathan, R. P. Viswanath and C. S. Gopinath, *Chem. Matter*, **2005**, 17, 6349 – 6353.

51. L. Jia, C. Wu, Y. Li, S. Han, Z. Li, B. Chi and J. Pu, *Appl. Phys. Lett*, **2011**, 98, 211903:1 -3

52. F. Rongrong, G. Shanmin, X. Hui, W. Qingyao and W. Zeyan, *RSC Adv,* **2014**, *4*, 37061-37069.

53. X. Zhigang, W. Hao Z. Luhong, G. Yi and X.S. Zhao, *J. Mater. Chem. A,* **2014**, *2*, 9291-9297.

54. N. Z. Wei, C. Z. Sheng, F. L. Ye and P. L. Zhi, *Chem. Sci,* **2015**, *6*, 3483-3494.

55. K. Ming, L. Yuanzhi, C. Xiong, T. Tingting, F. Pengfei, Z. Feng and Z. Xiujian, *J. Am. Chem. Soc,* **2011**, *133*, 16414- 16417.

56. Y. Junqing, W. Guangiun, G. Naijia, L. Landong, L. Zhuoxin and Z. C. Xing, *Phys. Chem. Chem. Phys,* **2013**, *15*, 10978-10988.

57. S. Grish Kumar and L. Gomathi Devi. *J. Phys. Chem. A,* **2011**, *115*, 13211-13241.

58. I. B. Roger, G. C. Teresita, S. L. John, P. Leonardo, T. Richard and J. D. Tilleyd, *J. Solid State Che,.* **1991**, *92*, 178-190.

59. C. H. Deanna, G. A. Alexander and A. G Kimberly, *J. Phys. Chem. B,* **2003**, *107*, 4545-4549.

60. F. L.Yan, X. Danhua, I.O. Jeong, S. X. L. Wenzhong and Y. Ying, *J. ACS Catal,* **2012**, *2*, 391-398.

61. D. Sarkar and K. K. Chattopadhyay, *ACS Appl. Mater. Interfaces,* **2014**, 6, 10044-10059.

62. D. Fan, Z. Weirong and W. Zhongbiao, *J. Nano.Technol,* **2008**, *19*, 365607-365617.

Figure Captions

Figure 1. XRD pattern (a) undoped and (b) C-N-S doped TiO_2 nanoparticles.

Figure 2. FTIR spectra (a) undoped and (b) C-N-S doped TiO_2 nanoparticles.

Figure 3. UV-Vis DRS spectra of (a) undoped and (b) C-N-S doped TiO_2 nanoparticles.

Figure 4. PL emission spectra of (a) undoped and (b) C-N-S doped TiO_2 nanoparticles with the excitation wavelengths of 290 nm.

Figure 5. PL emission spectra of (a) P4 and (b) D4 with different excitation wavelengths.

Figure 6. Rhodamine B dye degradation spectra of P4 and D4.

Figure 7. Dye degradation efficiency of undoped and C-N-S doped TiO_2 nanocatalysts.

Figure 8. Kinetics of Rh B degradation of P4 and D4.

Figure 9. UV- Vis spectral changes of Rh B as a function of irradiation time and wavelength shifts for P4 and D4.

Figure 10. Change of absorption variation for P4 and D4.

Figure 11. Electron migration in C-N-S doped TiO_2 with binary polymorphs.

Table Caption

Table 1. Crystallite size and lattice strain of the synthesized TiO_2 nanoparticles.

Table 2. Bandgap determination of undoped and C-N-S doped TiO_2 nanoparticles
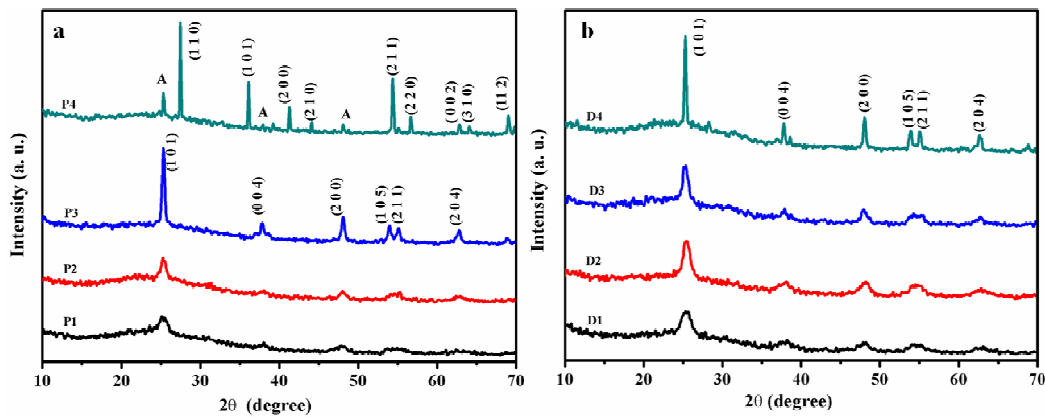
Figure 1.
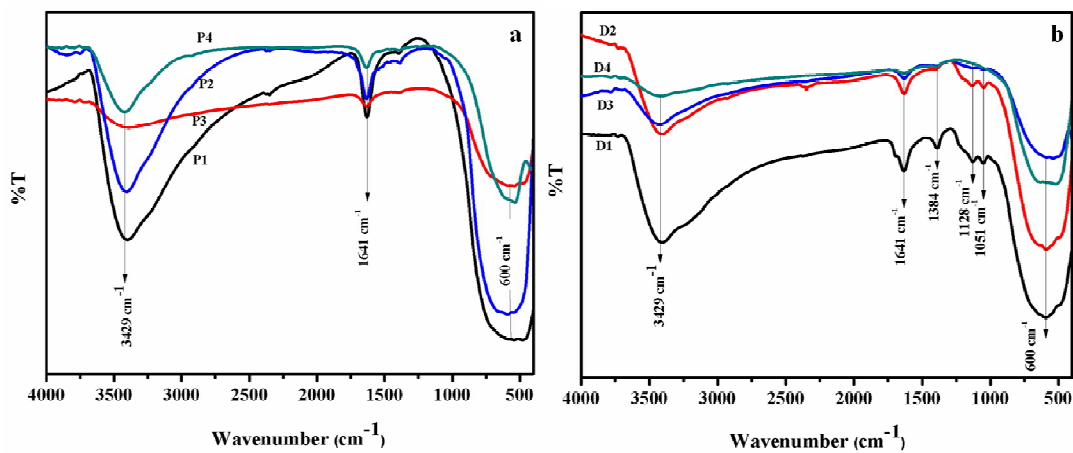
Figure 2.
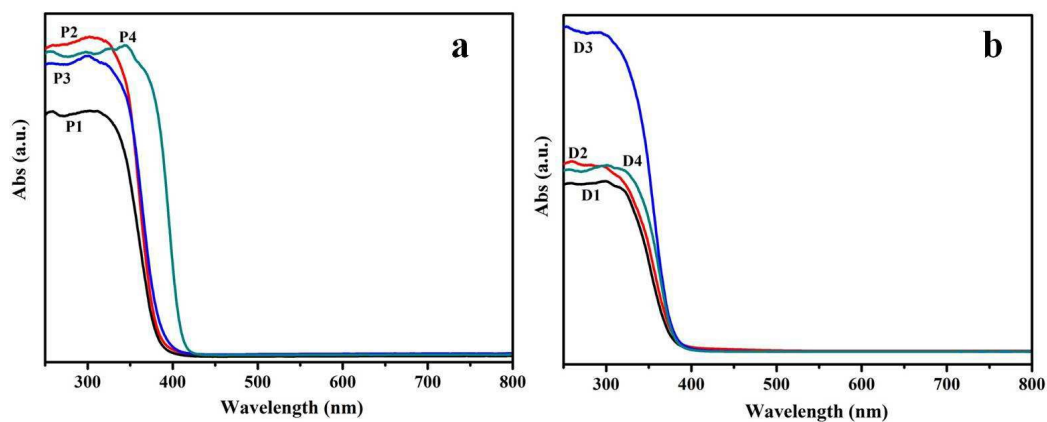
Figure 3.
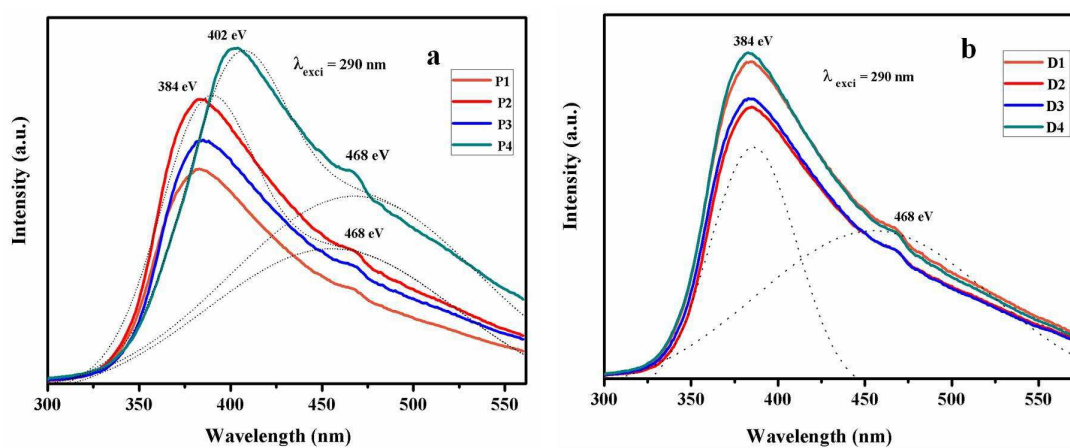
Figure 4.
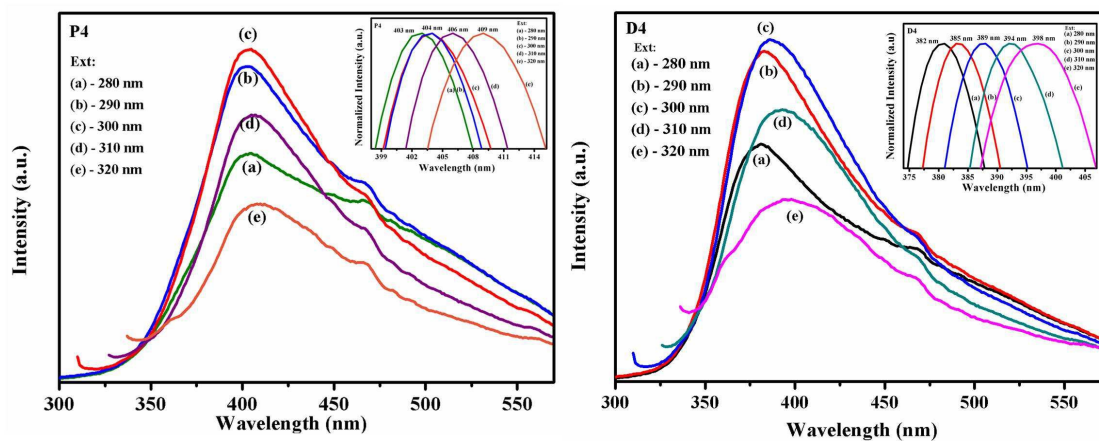
Figure 5.
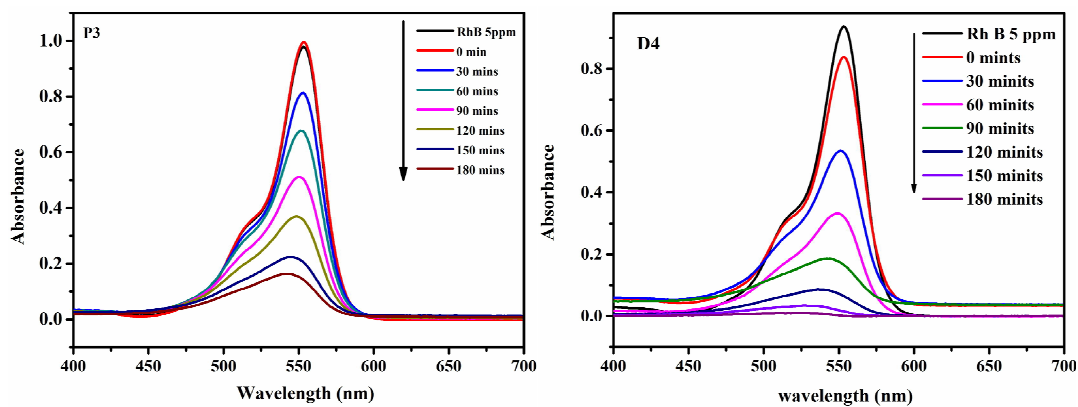
Figure 6.
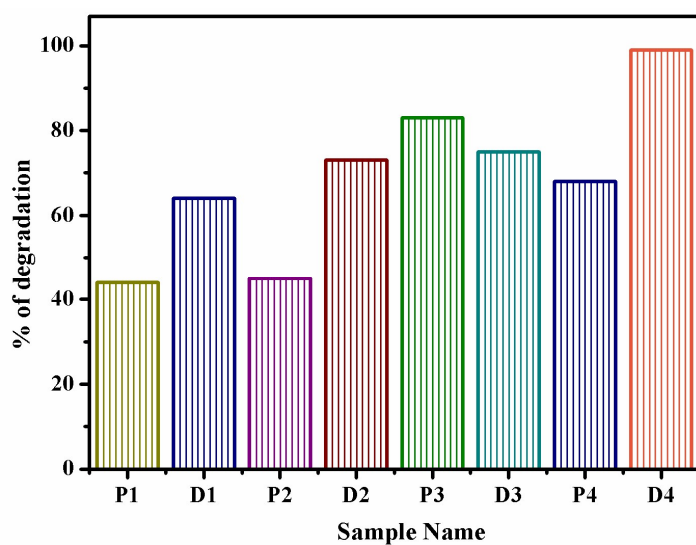
Figure 7.
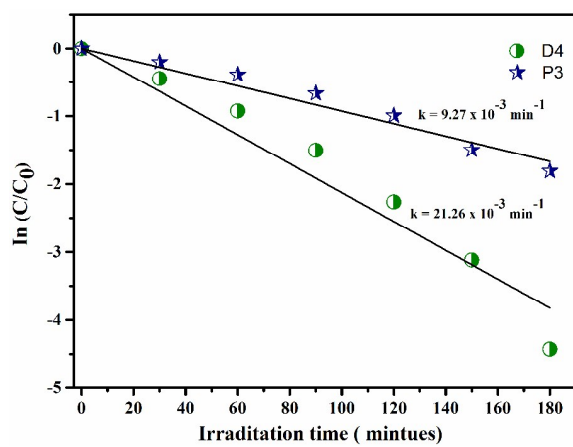
Figure 8.
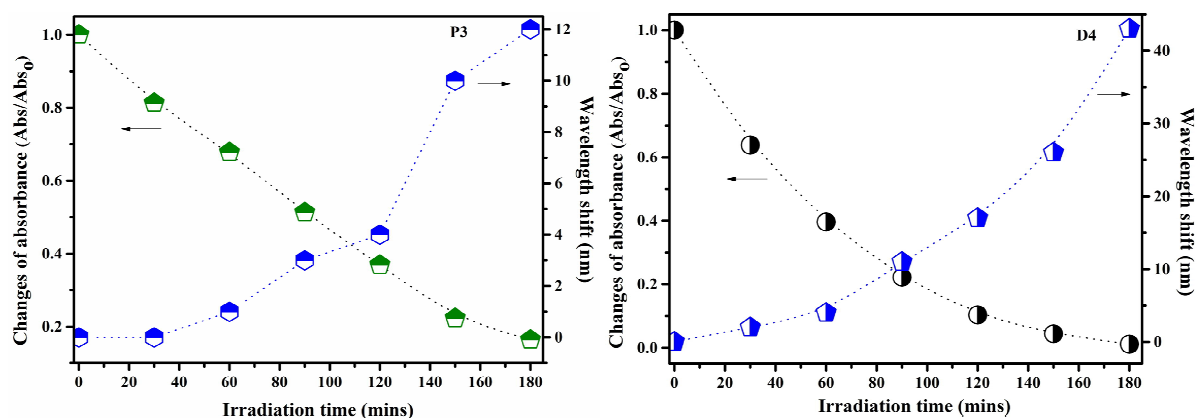
Figure 9.
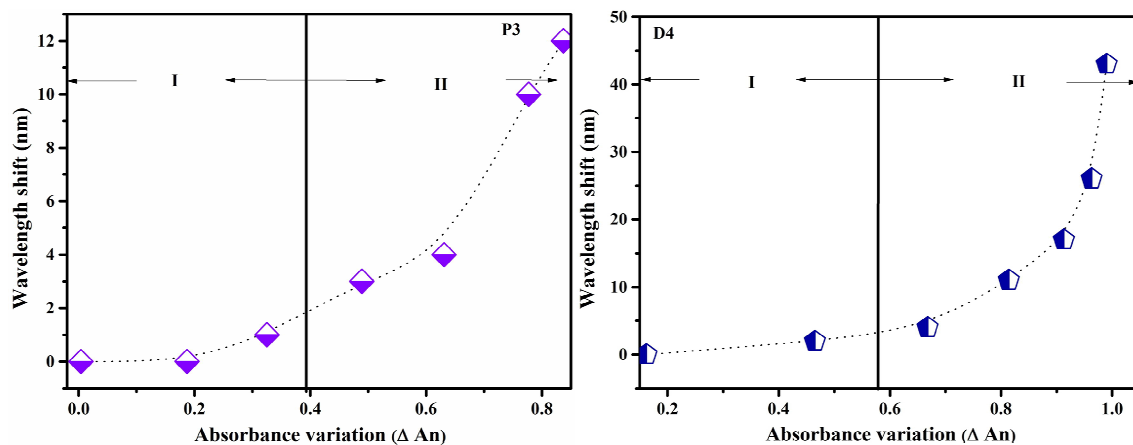
Figure 10.
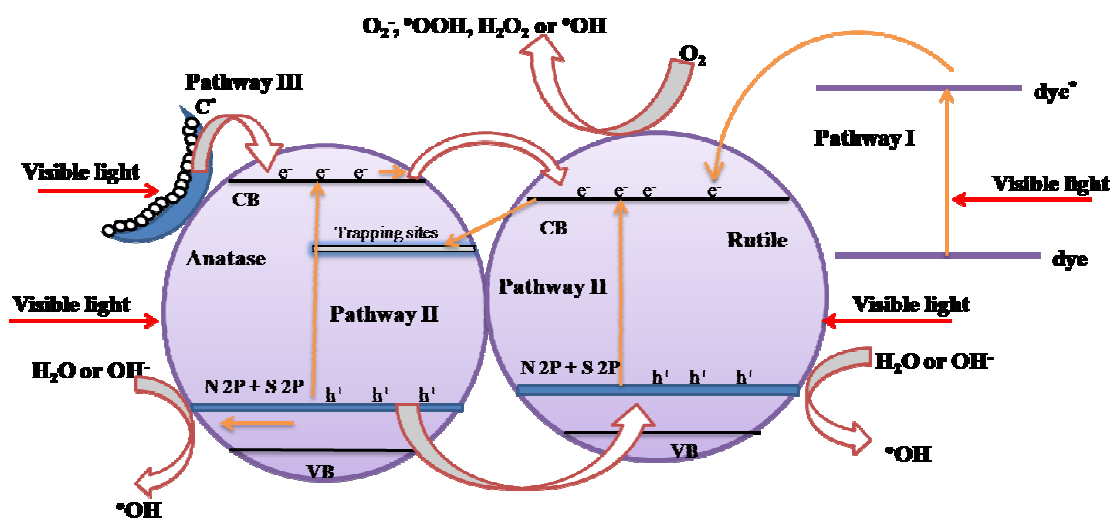
Figure 11.

Table 1.

Sample	Scherrer's Formula	Size-Strain Plot Method (SSP)			
	D (nm)	D (nm)	$\varepsilon \times 10^{-3}$	δ (MPa)	u (KPa)
P2	6	9	7.83	1303	5101
P3	19	28	1.60	261	208
P4	36	32	0.52	151	39
D2	5	10	11	1760	9506
D3	7	4	3.87	636	1233
D4	6	9	1.96	320	313

Table 2.

Sample	Absorbance Maximum	Kubelka- Munk Function – Bandgap (e.V)
P1	385	3.17
P2	384	3.17
P3	389	3.13
P4	413	2.94
D1	389	3.12
D2	386	3.14
D3	390	3.13
D4	391	3.12

Graphical Abstract